

Role of impurities on the optical properties of rectangular graphene flakes

Z. S. Sadeq,^{*} Rodrigo A. Muniz, and J. E. Sipe

Department of Physics, University of Toronto, 60 St. George Street, Toronto, Ontario, Canada, M5S 1A7



(Received 17 October 2017; published 16 January 2018)

We study rectangular graphene flakes using mean field states as the basis for a configuration interaction calculation, which allows us to analyze the low lying electronic excited states including electron correlations beyond the mean field level. We find that the lowest energy transition is polarized along the long axis of the flake, but the charge distributions involved in these transitions are invariably localized on the zigzag edges. We also investigate the impact of both short and long range impurity potentials on the optical properties of these systems. We predict that even a weak impurity localized at a zigzag edge of the flake can have a significant—and often dramatic—effect on its optical properties. This is in contrast to impurities localized at armchair edges or central regions of the flake, for which we predict almost no change to the optical properties of the flake even with strong impurity potentials.

DOI: [10.1103/PhysRevMaterials.2.014001](https://doi.org/10.1103/PhysRevMaterials.2.014001)

I. INTRODUCTION

Graphene has attracted tremendous interest due to its remarkable properties, such as its optical response, its mechanical strength, its zero band gap, and its thermal conductivity [1–10]. It has been used in a variety of optical applications, as a saturable absorber [11–14], polarizer [15], and mode locker [16]. Graphene nanoribbons also have interesting electronic and optical properties [17,18], in particular, ribbons with zigzag edges exhibit flat bands associated with edge states that give rise to unconventional optical properties of the nanoribbon [19,20]. Synthesis methods for graphene often result in small, finite sized byproducts, known as graphene flakes or graphene quantum dots, which can be smaller than 2 nm in diameter [21]. Some of these flakes have been synthesized and characterized in solution [22–24], while others have been deposited on substrates such as silicon carbide [25,26]. These finite sized flakes and other carbon based materials, with their nonzero energy gaps, have been discussed for possible electronic and optical device applications as graphene flake photodetectors, light-emitting diodes, and sensitizers in solar cells [27–29]. There are also proposed biomedical applications of graphene flakes, such as the imaging of cancer and stem cells, real time molecular tracking in live cells, and *in vivo* imaging of cellular processes [30]. Key to the development of graphene flakes for applications is the understanding of their optical properties. While the optical properties of graphene have been extensively studied [17,31–34] including some finite size [35–38] and impurity [39–42] effects, the optical properties of finite size graphene flakes have not been, partly due to the shortcomings of mean field theory in finite systems.

Previous studies [22,43–51] have demonstrated that the size and shape of graphene flakes, as well as the nature of their edges, have an impact on their optical properties. Early work [43,50,51] focused on hexagonal and triangular flakes with

either zigzag or armchair edges only. Recently, there has been some progress towards the synthesis of rectangular graphene flakes [52]. Rectangular flakes inevitably contain both types of edges and can display unique behavior due to the competition between effects associated with each kind of edge. Research on these flakes has so far been at the mean field level [49,53,54], and there is still little understanding of the optical properties of these flakes as the size of zigzag or armchair edges are increased.

It has been shown experimentally that common methods for generating graphene and graphene flakes can introduce a variety of localized impurities [55], and these impurities can have a significant effect on the electronic and optical properties. Progress has been made in detecting the location of impurities on graphene flakes [56]. While there has been some work done on how long-range disorder affects the absorption spectra of large armchair edge hexagonal graphene flakes [51], there has been little discussion of how localized impurities affect the electronic properties of graphene flakes more generally. An understanding of how impurities can be used to tune the optical properties of graphene flakes is important for optical device applications, such as saturable absorbers [11–14].

In this paper, we use an extended Hubbard model, also known as the Pariser-Parr-Pople (PPP) model [57–59], to describe the p_z electrons in these graphene flakes and apply the configuration interaction (CI) method to solve for the many-body states in these systems. We verify that including electron correlations beyond mean-field theory is essential. We show that varying the size of armchair or zigzag edges significantly changes the optical properties of these flakes, as well as the nature of the electron distribution involved in the optical transitions. We also investigate the effect of impurity potentials of various strengths and ranges in these systems and demonstrate that impurity potentials located on the zigzag edges can have a significant effect on the low energy absorption spectrum of these flakes. This is in contrast to impurities located near the center or on armchair edges of the flakes, which have an almost negligible impact on the

^{*}sadeqz@physics.utoronto.ca

absorption spectrum regardless of the strength and range of the impurity potential. Although the known results for nanoribbons suggest that the zigzag edge states should be prevalent in the low energy spectrum of large rectangular graphene flakes, our results confirm that even graphene flakes of very small sizes have mainly zigzag edge states in their low energy spectrum.

This paper is organized as follows: In Sec. II we present details on the model we have used to solve for the many-body states of graphene flakes, in Sec. III we calculate the absorption spectra of two different families of rectangular graphene flakes, in Sec. IV we detail the effects of impurities centered at various locations of the graphene flake, and in Sec. V we present our conclusions.

II. METHOD

In graphene and other conjugated organic systems, the p_z electrons on the carbon backbone are primarily responsible for the low energy physics, while the s , p_x , p_y electrons are primarily responsible for the mechanical stability of the system [60–62]. We model the p_z electrons in the graphene flakes using the Pariser-Parr-Pople (PPP) Hamiltonian [57–59,63–65]:

$$H = H_{TB} + H_{Hu} + H_{\text{ext}} + H_{\text{imp}}, \quad (1)$$

where H_{TB} is the tight-binding Hamiltonian, H_{Hu} is the Hubbard Hamiltonian, H_{ext} extends the Hubbard Hamiltonian, and H_{imp} is the impurity Hamiltonian,

$$H_{TB} = -t \sum_{(i,j),\sigma} c_{i\sigma}^\dagger c_{j\sigma}, \quad (2)$$

$$H_{Hu} = U \sum_i n_{i\uparrow} n_{i\downarrow}, \quad (3)$$

$$H_{\text{ext}} = \frac{1}{2} \sum_{\substack{i \neq j \\ \sigma \sigma'}} V_{ij} \left(n_{i\sigma} - \frac{1}{2} \right) \left(n_{j\sigma'} - \frac{1}{2} \right), \quad (4)$$

$$H_{\text{imp}} = \sum_{i\sigma} \bar{\epsilon}_i c_{i\sigma}^\dagger c_{i\sigma}. \quad (5)$$

Here $t = 2.66$ eV is the hopping parameter [66,67], σ is a spin label, i and j are site labels, and the angular brackets indicate sums over nearest neighbors only. The fermion creation and

annihilation operators are denoted, respectively, by $c_{i\sigma}^\dagger$ and $c_{i\sigma}$, so the electron number operator for spin σ and site i is $n_{i\sigma} = c_{i\sigma}^\dagger c_{i\sigma}$.

We set the on-site repulsion parameter to $U = 8.29$ eV for all calculations [53]. While some researchers [47–49,51] have used heavily screened values for U , we base our choice of this parameter on recent calculations of the Coulomb repulsion parameter in graphene [53,68,69]. The parameters we use in this paper have been shown to result in a semimetal solution for the ground state of graphenelike systems [70–72] and are also similar to values used in calculations for other organic systems [65]. We approximate the long-range Coulomb repulsion by the Ohno interpolation [65],

$$V_{ij} = \frac{U}{\sqrt{1 + (4\pi\epsilon_0 U \epsilon r_{ij}/e^2)^2}}, \quad (6)$$

where U is the on-site repulsion parameter, ϵ is a screening parameter, r_{ij} is the distance between sites i and j , $e = -|e|$ is the electronic charge, and ϵ_0 is the vacuum permittivity. We set $\epsilon = 5$ for all calculations, in accordance with other researchers who have utilized this value of the screening parameter to model the long range Coulomb repulsion in similar systems [22,53].

Several types of impurities can affect graphene flakes. Common synthetic routes for the manufacture of graphene can introduce metallic impurities that can latch onto particular sites [55]. Other impurities include the substitution of carbon atoms on the edges of the graphene flake by boron and oxygen atoms [73,74]. To first approximation these impurities can be modeled by introducing a site dependent potential. We model the potential at \mathbf{r}_i due to an impurity at \mathbf{r}_c by a Gaussian

$$\bar{\epsilon}_i = \bar{\epsilon}_{\text{max}} \exp\left(-\frac{(\mathbf{r}_i - \mathbf{r}_c)^2}{2\tau^2}\right), \quad (7)$$

where τ characterizes the range of the impurity potential, \mathbf{r}_i is the location of site i , and $\bar{\epsilon}_{\text{max}}$ is the maximum value of the energy. While a range of these parameters are considered below, the default parameters we use to model the impurity potential are $\bar{\epsilon}_{\text{max}} = t/3$ and $\tau = l_b$. These parameters are in line with recent work done on modeling disorder in large graphene flakes [51].

We first solve the Hartree-Fock (HF) equations for the PPP Hamiltonian (1),

$$\begin{aligned} H^{\text{HF}} = & -t \sum_{(i,j),\sigma} c_{i\sigma}^\dagger c_{j\sigma} + \sum_{i\sigma} \bar{\epsilon}_i c_{i\sigma}^\dagger c_{i\sigma} \\ & + U \sum_i ((n_{i\uparrow})n_{i\downarrow} + \langle n_{i\downarrow} \rangle n_{i\uparrow} - \langle n_{i\uparrow} \rangle \langle n_{i\downarrow} \rangle - \langle c_{i\uparrow}^\dagger c_{i\downarrow} \rangle \langle c_{i\downarrow}^\dagger c_{i\uparrow} \rangle - \langle c_{i\downarrow}^\dagger c_{i\uparrow} \rangle \langle c_{i\uparrow}^\dagger c_{i\downarrow} \rangle + \langle c_{i\uparrow}^\dagger c_{i\downarrow} \rangle \langle c_{i\downarrow}^\dagger c_{i\uparrow} \rangle) \\ & + \sum_{i \neq j} V_{ij} \left(n_i \langle n_j \rangle - n_i - \frac{1}{2} \langle n_i \rangle \langle n_j \rangle + \frac{1}{2} - \frac{1}{2} \sum_{\sigma \sigma'} \langle c_{i\sigma}^\dagger c_{j\sigma'} \rangle \langle c_{j\sigma'}^\dagger c_{i\sigma} \rangle + \langle c_{j\sigma'}^\dagger c_{i\sigma} \rangle \langle c_{i\sigma}^\dagger c_{j\sigma'} \rangle - \langle c_{i\sigma}^\dagger c_{j\sigma'} \rangle \langle c_{j\sigma'}^\dagger c_{i\sigma} \rangle \right). \quad (8) \end{aligned}$$

This equation is derived following the prescription found in standard references [53,75–77]. We diagonalize (8) self consistently, using the tight-binding (2) eigenfunctions as an initial guess. For the parameters used, we find two stable

solutions: one antiferromagnetic and one paramagnetic. The antiferromagnetic solution is discarded [71,72,78–81], since other methods that treat electron correlation more rigorously than HF, such as quantum Monte Carlo and CI calculations,

have shown that the paramagnetic solution [70,82,83] is the lower energy state on similar but smaller systems. Upon the self-consistent solution of (8) with paramagnetic expectation values, one can write (8) in its diagonal form

$$H^{\text{HF}} = \sum_{m\sigma} \hbar\omega_{m\sigma} C_{m\sigma}^\dagger C_{m\sigma}, \quad (9)$$

where $\hbar\omega_{m\sigma}$ are the eigenvalues associated with the single particle states. The operators $C_{m\sigma}^\dagger$ and $C_{m\sigma}$ can be written in terms of the site basis as

$$C_{m\sigma}^\dagger = \sum_i M_{m\sigma,i} c_{i\sigma}^\dagger, \quad (10)$$

$$C_{m\sigma} = \sum_i M_{m\sigma,i}^* c_{i\sigma}, \quad (11)$$

where $C_{m\sigma}^\dagger$ indicates the creation of a HF quasiparticle in state m with spin σ , $M_{m\sigma,i}$ is the amplitude associated with the state m at site i , and is typically nonzero for all i .

The single particle states obtained from solving the HF equations with paramagnetic expectation values self consistently are then used to construct the HF ground state

$$|g_{\text{HF}}\rangle = \prod_m^{N/2} C_{m\uparrow}^\dagger C_{m\downarrow}^\dagger |\text{vac}\rangle, \quad (12)$$

where $|\text{vac}\rangle$ represents the full vacuum, and N is the number of electrons in the system. The states that are filled in the HF ground state are denoted as ‘‘valence,’’ and those that are unfilled in the HF ground state are denoted as ‘‘conduction.’’

We then rewrite the total Hamiltonian (1) in the HF electron-hole basis; its full form is given in Appendix. We use an electron-hole basis, where the HF electron creation is designated by the operator $a_{L_m\sigma}^\dagger$, and the HF hole creation is designated by the operator $b_{H_n\sigma}^\dagger$, so

$$a_{L_m\sigma} = C_{L_m\sigma}, \quad b_{H_n\sigma}^\dagger = C_{H_n\bar{\sigma}}, \quad (13)$$

where $\bar{\sigma}$ is the opposite spin of σ , L_m is the m th state above the lowest unoccupied HF state, and H_n is the n th state below the highest occupied HF state. The lowest unoccupied HF state itself is denoted as L_0 and the highest occupied HF state itself is denoted as H_0 , or for simplicity, L and H , respectively.

We select an ‘‘active space’’ for our CI calculation defined by a set of HF excited states, identified by overbars. The singly excited states are of the form

$$|\overline{L_m H_n}; \sigma\rangle = a_{L_m\sigma}^\dagger b_{H_n\bar{\sigma}}^\dagger |g_{\text{HF}}\rangle, \quad (14)$$

where m, n range over $\{0, \dots, 4\}$. The doubly excited states are of the form

$$|\overline{L_m L_{m'}; H_n H_{n'}}\rangle = a_{L_m\uparrow}^\dagger a_{L_{m'}\downarrow}^\dagger b_{H_n\downarrow}^\dagger b_{H_{n'}\uparrow}^\dagger |g_{\text{HF}}\rangle, \quad (15)$$

where m, m', n, n' all range over $\{0, \dots, 4\}$. In the special case where $m = m'$ and $n = n'$ we write $|\overline{2L_m H_n}\rangle$ for $|\overline{L_n L_n}; H_n H_n\rangle$. Together with the HF ground state (12), these HF excited states are used to approximately diagonalize the total Hamiltonian (1). Upon diagonalization of the many-body Hamiltonian (1), the states become superpositions of the HF

states; for example, the ground state is given by

$$|g\rangle = f_g^{GS} |g_{\text{HF}}\rangle + \sum_{\alpha,\beta,\sigma} f_g^{\alpha\beta\sigma} |\overline{L_\alpha H_\beta}; \sigma\rangle + \sum_{\alpha\beta\gamma\delta} f_g^{\alpha\beta\gamma\delta} |\overline{L_\alpha L_\beta; H_\gamma H_\delta}\rangle, \quad (16)$$

where f_g^{GS} , $f_g^{\alpha\beta\sigma}$, $f_g^{\alpha\beta\gamma\delta}$ are the CI ground state amplitudes of the HF ground state, single excitations, and double excitations, respectively. The excited states have similar expressions. We do not include higher order excitations in our calculation because their energies are large compared to the single and double excitations that are included, so their contribution to the CI low energy states can be expected to be small; as well, the matrix elements of the Hamiltonian between the HF ground state and the states with higher order excitations vanish. For the systems of interest, the main contribution to the CI ground state (16) is from the HF ground state, as it corresponds to more than half ($|f_g^{GS}|^2 > 0.5$) for all the systems studied in this paper, indicating that the HF ground state is indeed a good starting point. We find that increasing the active space in our calculation does not significantly change the composition of the low energy states, indicating that our calculation already includes all relevant HF excitations that make up the low energy states of the system.

Absorption spectrum calculation

In this subsection, we outline the calculation for the first order polarizability of the system and introduce the spatial profile of the transition, a quantity which is used to characterize the charge distributions of electronic states involved in bright transitions. The number operator for a particular site i is defined as

$$n_i = \sum_\sigma c_{i\sigma}^\dagger c_{i\sigma}. \quad (17)$$

In the electron-hole basis, it is written as

$$n_i = \sum_{mm'\sigma} \Gamma_{mm'\sigma,i} (a_{m\sigma}^\dagger a_{m'\sigma} - b_{m'\sigma}^\dagger b_{m\sigma}) + \sum_{mm'\sigma} \Gamma_{mm'\sigma,i} (a_{m\sigma}^\dagger b_{m'\bar{\sigma}}^\dagger + b_{m\bar{\sigma}} a_{m'\sigma}) + \sum_{m\sigma} \Gamma_{mm\sigma,i}, \quad (18)$$

where we have defined

$$\Gamma_{mm'\sigma,i} = M_{m\sigma,i} M_{m'\sigma,i}^*, \quad (19)$$

and $M_{m\sigma,i}$ is the amplitude of the HF state m with spin σ at site i .

The dipole moment operator is approximated as

$$\boldsymbol{\mu} = \sum_i e \mathbf{r}_i \left(\sum_\sigma c_{i\sigma}^\dagger c_{i\sigma} - 1 \right), \quad (20)$$

where the charge of each nucleus not balanced by the in-plane bonding electrons of the molecule is included, and so the dipole moment operator is independent of origin. Transforming it into the electron-hole basis as defined in the previous subsection,

we have

$$\begin{aligned} \boldsymbol{\mu} = & \sum_{m\sigma} \boldsymbol{\mu}_{mm\sigma} - e \sum_i \mathbf{r}_i + \sum_{mm'\sigma} \boldsymbol{\mu}_{mm'\sigma} a_{m\sigma}^\dagger a_{m'\sigma} \\ & - \sum_{mm'\sigma} \boldsymbol{\mu}_{mm'\sigma} b_{m'\sigma}^\dagger b_{m\sigma} + \sum_{mm'\sigma} \boldsymbol{\mu}_{mm'\sigma} a_{m\sigma}^\dagger b_{m'\sigma}^\dagger \\ & + \sum_{mm'\sigma} \boldsymbol{\mu}_{mm'\sigma} b_{m\sigma} a_{m'\sigma}, \end{aligned} \quad (21)$$

where

$$\boldsymbol{\mu}_{mm'\sigma} = \sum_i e \mathbf{r}_i M_{m\sigma,i} M_{m'\sigma,i}^*. \quad (22)$$

We determine the absorption spectrum by calculating the imaginary component of the first order polarizability of the system [84]. Assuming the system is initially in the ground state, the imaginary component of the first order polarizability is given by

$$\text{Im}(\alpha_{kl}^{(1)}(\omega)) = \frac{\gamma}{\epsilon_0 \hbar} \sum_n \frac{\mu_{gn}^k \mu_{ng}^l}{(\omega_{ng} - \omega)^2 + \gamma^2}, \quad (23)$$

where k, l are Cartesian components, μ_{gn} is the matrix element of the dipole moment operator between the ground state and the state n , and $\hbar\gamma$ is a frequency broadening, which we set to $\hbar\gamma = 0.01$ eV for all calculations, primarily for reasons of presentation [85].

In order to analyze the charge distributions of electronic states involved in bright transitions, we define

$$T_{Y,i} = \langle g | n_i | Y \rangle, \quad (24)$$

where i is the site, g is the CI ground state, and Y is a CI excited state. This quantity is related to the matrix element of the dipole moment operator between the ground state and Y , the “transition dipole moment,”

$$\langle g | \boldsymbol{\mu} | Y \rangle = \sum_i e \mathbf{r}_i T_{Y,i}. \quad (25)$$

We call $T_{Y,i}$, taken as a function of i for fixed Y , the spatial profile of the transition $g \rightarrow Y$.

III. PRISTINE GRAPHENE FLAKES

We first investigate the optical properties of the pristine graphene flakes. In this section, we present our calculations for the absorption spectra of the two families of pristine graphene flakes and observe the trends as we increase their size. We also present the spatial profiles of a select few low energy transitions. For the rest of this paper, we shall refer to the HF single particle levels as “modes,” and we shall refer to a state that results from the CI calculation as a “state.” In these systems, the highest occupied HF mode and the lowest unoccupied HF mode primarily have electron density concentrated on the zigzag edges of the flake and are labeled as edge modes. Modes that are below (above) the highest occupied HF mode (lowest unoccupied HF mode) typically have electron density spread throughout the flake, and are labeled as bulk modes. We label the lowest energy bright excited state the S_1 state, and the second lowest energy bright excited state the S_2 state, and so on.

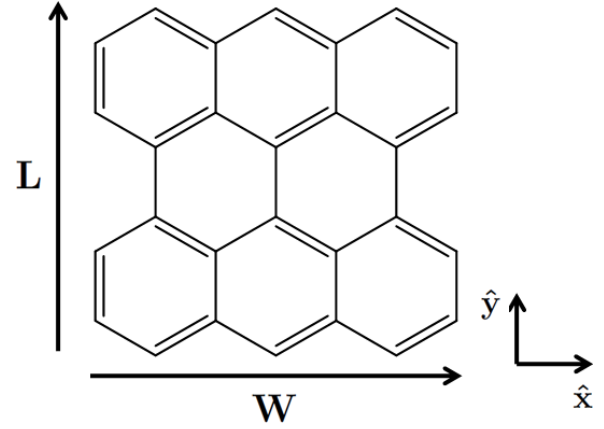


FIG. 1. A cartoon illustration of the W3L3 flake. Here the width and length of this flake are both composed of three hexagons. The axis convention used in the rest of the paper is also illustrated in this figure; the width corresponds to the \hat{x} axis, and the length corresponds to the \hat{y} axis.

We investigate rectangular graphene flakes, and use two numbers to specify a particular rectangular graphene flake: the “width,” which identifies the number of hexagons on the horizontal axis, and the “length,” which identifies the number of hexagons on the vertical axis of this flake. The notation we use is $WwLl$ for a flake with a width of w hexagons and a length of l hexagons. The width corresponds to the size of the zigzag edges, while the length corresponds to the size of the armchair edges of the flakes. We illustrate the example of the W3L3 flake in Fig. 1. The four families of flakes we consider are the $W3Ln$, $WnL3$, $W5Ln$, and $WnL5$ families. The $W3Ln$ family consists of all flakes where the width is 3 hexagons but the length varies, e.g., W3L3, W3L5, ..., W3L11; in this family of flakes the armchair edges are larger than the zigzag edges. The $WnL3$ family consists of all flakes where the length is 3 hexagons but the width varies, e.g., W3L3, W5L3, ..., W11L3; in this family of flakes the zigzag edges are larger than the armchair edges. The $W5Ln$ family consists of all flakes where the width is 5 hexagons but the length varies, e.g., W5L5, W5L7, and W5L9; in this family of flakes the armchair edges are larger than the zig-zag edges. Finally, the $WnL5$ family consists of all flakes where the length is 5 hexagons but the width varies, e.g., W5L5, W7L5, and W9L5; in this family of flakes the zigzag edges are larger than the armchair edges.

We first consider the $W3Ln$ family of flakes. In Fig. 2, we show the absorption spectrum for the $W3Ln$ family of flakes. As the size of the flake is increased, the first absorption peak is redshifted, as one would expect even within a noninteracting description of these flakes [17,65]. The first absorption peak corresponds to a transition dipole moment that is always polarized along the long (here \hat{y}) axis of the flake. We show a plot of $T_{S_1,i}$ for the W3L11 flake in Fig. 2. For this plot, and all subsequent plots of the spatial profiles of the transitions, we place a circle at the location of each site i ; the area of each circle indicates the magnitude of $T_{S_1,i}$, and the color indicates whether it is positive (red) or negative (blue). Even though in this family of flakes the size of the armchair edges is larger than the size of the zigzag edges, $T_{S_1,i}$ has electron concentration primarily on the zigzag edges. Although based on the results

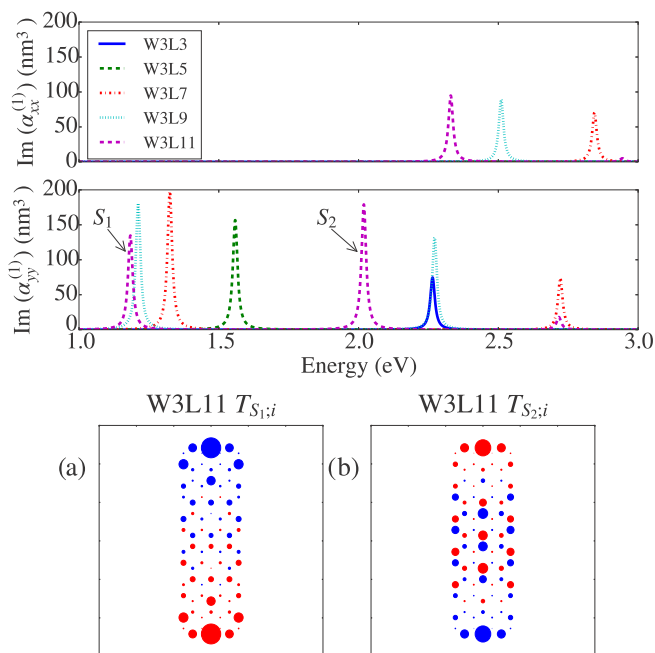


FIG. 2. (Top) Absorption spectrum of the $W3L_n$ family of flakes. As we consider larger flakes, the first absorption peak, associated with a transition with a transition dipole moment polarized along the long axis (here \hat{y}) of the flake, is redshifted. (Bottom) A plot of (a) $T_{S_1;i}$ and (b) $T_{S_2;i}$ in the $W3L11$ system. For the plots of $T_{S_1;i}$ and $T_{S_2;i}$, we place a circle at the location of each site i ; the area of each circle indicates the magnitude of the relevant quantity, and the color indicates whether it is positive (red) or negative (blue). The majority of the electron concentration is confined to the zigzag edges for both transitions.

of graphene nanoribbons it is expected that the electron concentration associated with the lowest energy absorption peak would be localized on the zigzag edges of the flakes, we find that this holds true even for the smallest graphene flake we consider. The dominant contributions to the S_1 state are from single excitations (14) of HF quasiparticles from the highest occupied HF mode to the lowest unoccupied HF mode—two modes that primarily have electron concentration on the zigzag edges—with some corrections from excitations of HF quasiparticles from the bulk modes. The second absorption peak is associated with a transition whose transition dipole moment is also polarized along the long axis (\hat{y}) of the flake. We show a plot of $T_{S_2;i}$ for the $W3L11$ flake in Fig. 2. Similar to $T_{S_1;i}$, $T_{S_2;i}$ also has significant electron concentration on the zigzag edges. The dominant contributions to the S_2 state are from double excitations (15) of HF quasiparticles, primarily involving excitations between edge modes.

In Fig. 3, we plot the absorption spectrum for the W_nL3 family of flakes. Again, as the flake gets larger, the first absorption peak is redshifted. For larger flakes, the first absorption peak is associated with a transition with a transition dipole moment polarized along the long axis (here \hat{x}) of the flake. We also plot $T_{S_1;i}$ for the $W11L3$ flake in Fig. 3. For the first bright excited state, $T_{S_1;i}$ indicates that the electrons involved in that particular transition are localized on the zigzag edges. The first bright excited state is composed of several HF double

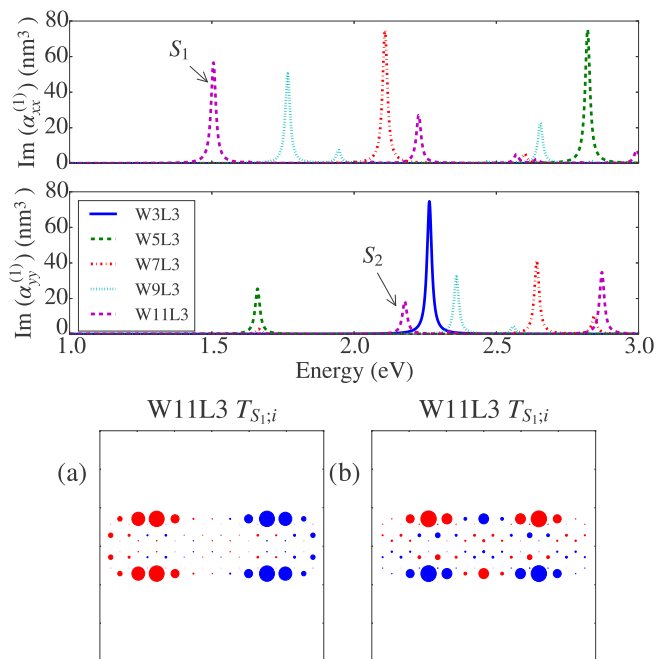


FIG. 3. (Top) Absorption spectrum of the W_nL3 family of flakes. Like the $W3L_n$ family, for the large flakes ($n > 5$) the first absorption peak is associated with a transition whose transition dipole moment is polarized along the long direction (here \hat{x}) of the flake. As the size of the system increases, the first absorption peak is redshifted. (Bottom) A plot of (a) $T_{S_1;i}$ and (b) $T_{S_2;i}$ in the $W11L3$ system. The majority of the electron concentration is confined to the zigzag edges for both transitions.

excitations. These states become bright because the CI ground state of these flakes has significant contributions from HF double excitations, which leads to a nonzero transition dipole moment between the ground state and the S_1 state. Unlike the $W3L_n$ family of flakes, the state which predominantly involves the HF single excitation between edge modes, the S_2 state in the W_nL3 family, is weakly bright and higher in energy than the first excited state. This optical transition is weak because the dominant contribution to the excited state, the HF single excitation which involves the transition from the edge modes, has a transition dipole moment which is oriented on the short axis (here \hat{y}) of the flake. The quantity $T_{S_2;i}$ is plotted in Fig. 3; it shows significant electron concentration on the zigzag edges of the system. In the $W3L_n$ family, the S_1 state is composed primarily of HF single excitations, while the S_2 state is composed mainly of HF double excitations. However, in the W_nL3 family this trend is reversed. These features cannot be observed using mean-field calculations only [53] and require the CI calculation.

We now turn to the $W5L_n$ family of flakes. In Fig. 4, we plot the absorption spectrum for the $W5L_n$ family of flakes. Both the first absorption peak, associated with a very weak transition whose transition dipole moment is polarized along the long axis (here \hat{y}) of the flake, and the second and much stronger absorption peak, associated with a transition whose transition dipole moment is polarized along the short axis (here \hat{x}), are redshifted as the flake gets larger. We plot $T_{S_1;i}$ in Fig. 4. For this particular system, $T_{S_1;i}$ extends around the

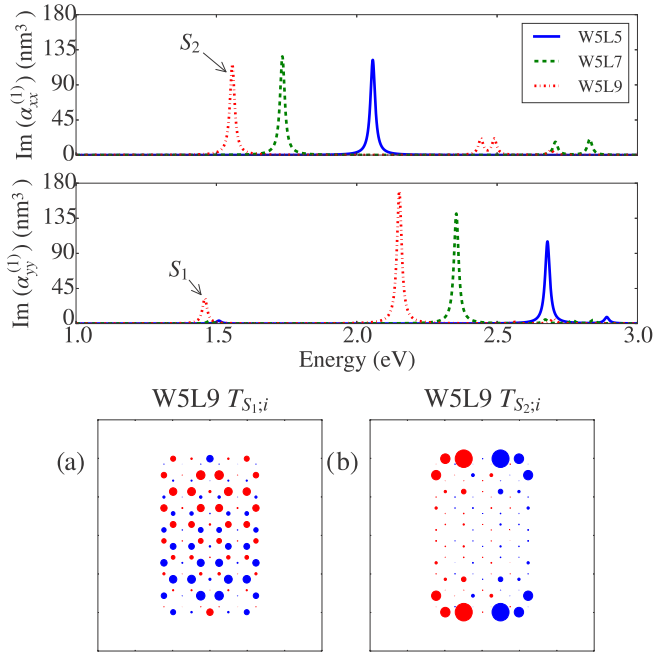


FIG. 4. (Top) Absorption spectrum of the $W5L_n$ family of flakes. As we consider larger flakes, the first two absorption peaks are redshifted. The lowest energy peak is associated with a transition with a transition dipole moment polarized along the long axis (here \hat{y}) of the flake, while the second lowest energy peak corresponds to a transition with a transition dipole moment polarized along the short axis (here \hat{x}) of the flake. (Bottom) Plot of (a) $T_{S_{1;i}}$ and (b) $T_{S_{2;i}}$ for the $W5L9$ system. The majority of the electron concentration is confined to the zigzag edges for the brighter transition ($g \rightarrow S_2$).

entire flake, although with a significant contribution from the zigzag edges. We also plot $T_{S_{2;i}}$ in Fig. 4, which shows that the electrons are concentrated almost exclusively on the zigzag edges of the system for this transition. In these flakes, the S_1 state is primarily composed of HF single excitations involving transitions from the edge modes, while for larger flakes, the S_1 state also has significant contributions from HF single excitations involving the bulk modes. This mixing is larger in these flakes than in the $W3L_n$ family. The S_2 state is primarily composed of HF double excitations.

The $W5L_n$ family of flakes behaves similarly to the $W3L_n$ family of flakes, except in the strength of the first absorption peak. This weak absorption peak, associated with a transition whose transition dipole moment is polarized along the long axis of the flake, is dwarfed in intensity by the bright peak associated with a transition whose transition dipole moment is polarized along the short axis.

Finally we investigate the W_nL5 family of flakes. We plot the absorption spectrum for these flakes in Fig. 5. As the flake gets larger, the first absorption peak is again redshifted, but unlike the $W5L_n$ family of flakes, the lowest absorption peak is very strong. The lowest absorption peak corresponds to the ground to S_1 transition, the associated transition dipole moment is polarized along the long axis (here \hat{x}) of the flake. The second lowest energy absorption peak corresponds to the ground to S_2 transition, the associated transition dipole moment is polarized along the short axis (here \hat{y}) of the flake. We

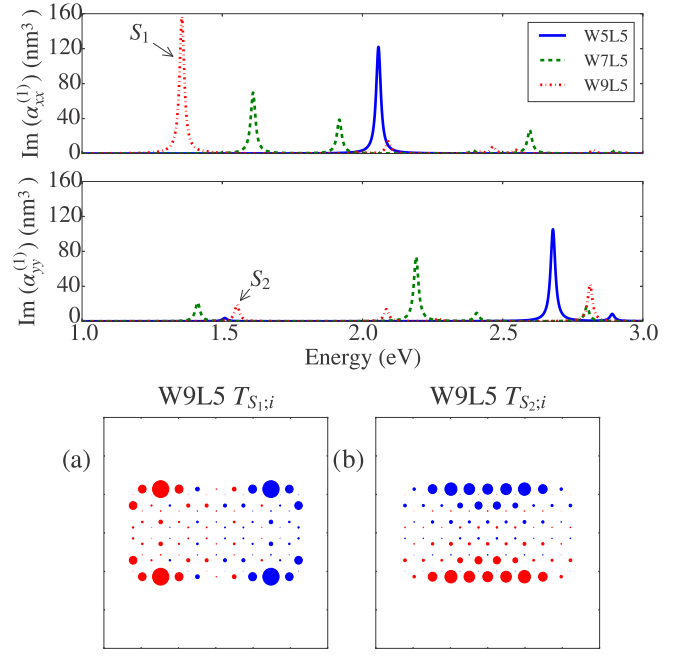


FIG. 5. (Top) Absorption spectrum of the W_nL5 family of flakes. As we consider larger flakes, the first two absorption peaks are redshifted. For the largest flake, $W9L5$, the lowest energy peak corresponds to a transition with a transition dipole moment oriented along the long axis (here \hat{x}) of the system, while the second lowest energy peak is attributed to a relatively weak transition with a transition dipole moment oriented along the short (here \hat{y}) axis of the flake. (Bottom) Plot of (a) $T_{S_{1;i}}$ and (b) $T_{S_{2;i}}$ for the $W9L5$ system. The electrons are concentrated on the zigzag edges for both these transitions.

plot $T_{S_{1;i}}$ and $T_{S_{2;i}}$ for the $W9L5$ flake in Fig. 5. For both these states, most of the electron concentration is located on the zigzag edges. Unlike the $W5L_n$ family of flakes, the S_1 state in the W_nL5 family is composed mainly of several HF double excitations, while the S_2 state is composed primarily of HF single excitations involving transitions between edge modes, but with significant mixing from HF single excitations involving transitions between bulk modes. The trends we see in the W_nL5 family are similar to the W_nL3 family, for which the lowest energy bright state is composed of mainly HF double excitations while the second lowest energy bright state is composed mainly of HF single excitations.

In summary, the lowest energy bright transition for pristine graphene flakes invariably has a transition dipole moment polarized along the long axis of the flake. When the armchair edges are larger than the zigzag edges, the lowest energy bright excited state is composed mainly of HF single excitations. However, when the zigzag edges are larger than the armchair edges, the lowest energy bright excited state is composed mainly of HF double excitations.

We conclude this section by comparing the predictions of our CI calculation with those that would follow from a simple mean field approach. As an example, in Fig. 6 we consider the $W11L3$ flake. For each method, we present the predicted absorption spectrum and the spatial profile of the first bright transition. There are large discrepancies between

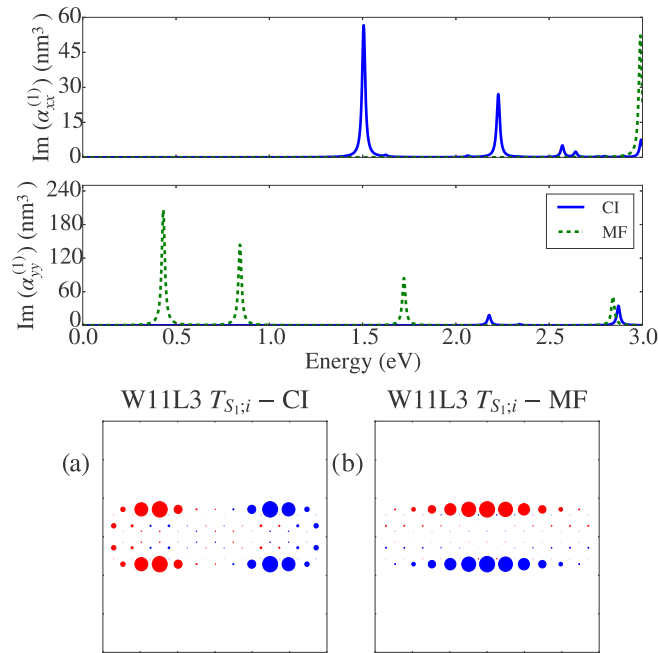


FIG. 6. (Top) Absorption spectrum of the W11L3 flake from the CI calculation and the mean field (MF) calculation. (Bottom) Plot of (a) $T_{S_i,i}$ for the CI calculation and (b) $T_{S_i,i}$ for the MF calculation for the W11L3 flake.

the two methods. Besides the large differences in the calculated transition energies, the mean field calculation indicates that the first absorption peak for both of these flakes is associated with a transition dipole moment polarized along the short (here \hat{y}) axis while the CI calculation identifies it with one polarized along the long (here \hat{x}) axis. In the CI calculation, the excited states are superpositions of several HF excitations; this leads to CI excited states that are qualitatively different from the excited states predicted by mean field theory alone.

IV. THE EFFECTS OF IMPURITIES ON THE ABSORPTION SPECTRA

Impurities can impact the optical properties of graphene flakes depending on the location, strength, and range of influence of the impurity potentials [21,25,26,55]. In this section, we analyze the effect of impurities on the optical properties of the graphene flake families discussed in the previous section. We consider impurity potentials centered on the zigzag edges, armchair edges, and in the center of the flake, and compute the optical properties of the graphene flake. We illustrate these impurity potentials in Fig. 7. We show results for positive impurity potentials. Changing the sign of the impurity potential does not qualitatively change the results presented in this section. This can be understood by treating the impurity potential perturbatively. The first order correction to the energy of states, given by $\langle \psi | H_{\text{imp}} | \psi \rangle$ where ψ corresponds to a particular CI state, is similar for the ground state and states close in energy to it. This is due to the fact that the densities associated with the ground state and the low energy unperturbed states are approximately similar around the

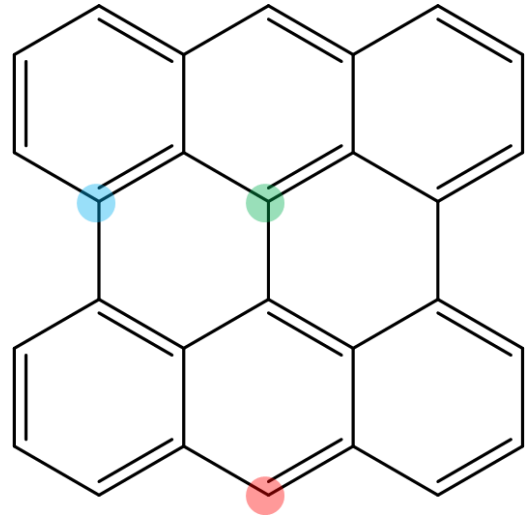


FIG. 7. Cartoon of a W3L3 flake showing the locations of various impurity potentials. The red circle represents an impurity placed on the zigzag edges, the light blue circle represents an impurity placed on the armchair edges, and the green circle represents an impurity placed in the middle, or so-called “bulk” region, of the flake.

impurity location. Therefore, the effect of impurity potentials becomes significant only at second order in the perturbation, for which the energy corrections are independent of the sign of the impurity potential.

We first examine a flake with larger armchair edges than zigzag, namely the W3L11 flake. The absorption spectrum of the W3L11 flake, with a Gaussian impurity potential located on the middle, armchair, and zigzag edges of the flakes are plotted in Fig. 8. We use the impurity potential parameters $\bar{\epsilon}_{\text{max}} = t/3$ and $\tau = l_b$, for which the absorption spectra of the flakes with the impurity on its armchair edge or in the center of the flake are unchanged from that of the pristine graphene flake. The low-lying bright excited states are not significantly affected

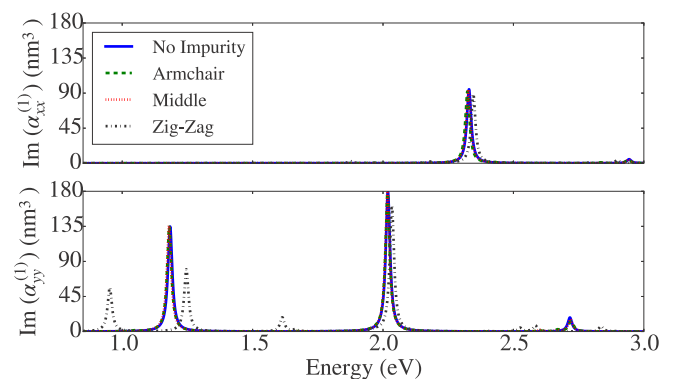


FIG. 8. Absorption spectrum of the W3L11 flake with varied impurity locations. The absorption remains unchanged for impurity potentials centered on the armchair edges or in the middle of the flake, but placing an impurity potential on one of the zigzag edges results in two new low energy peaks, one redshifted, one blueshifted from the original absorption line. The parameters used to model the impurity potential were $\bar{\epsilon}_{\text{max}} = t/3$ and $\tau = l_b$.

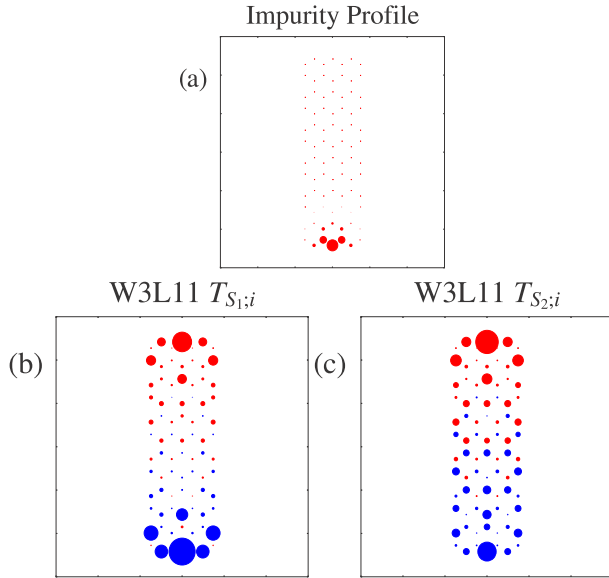


FIG. 9. (a) Profile of an impurity placed in the zigzag bottom site of the W3L11 flake. Plot of (b) $T_{S_{1,i}}$ and (c) $T_{S_{2,i}}$ for the W3L11 system with an impurity potential from (a). The charge distributions for these transitions are still concentrated around the zigzag edges. The parameters used to model the impurity potential were $\bar{\epsilon}_{\max} = t/3$ and $\tau = l_b$.

by the presence of the impurity potential on these locations, as evidenced by the absorption spectrum and the joint density of states. This is because the spatial profiles of the low lying excitations have little electron concentration on the armchair edges or in the middle of the flake. As illustrated in the previous section, the low energy transitions in rectangular graphene flakes have electron concentration on the zigzag edges. The electron concentration on the zigzag edges is unaffected by impurity potentials centered on the middle or armchair edges of the flake, unless the impurity potentials extend to the zigzag edges.

In contrast, an impurity on a zigzag edge of a graphene flake can have a significant impact on its optical properties. This is because the charge distributions involved in the bright transitions have significant concentration on the zigzag edges. The impurity blueshifts the first absorption peak, as the excited state involved in the transition becomes less energetically favorable due to the presence of the impurity potential. It also mixes a dark transition with a bright HF single excitation that involves an excitation of an electron between the edge modes. In Fig. 9, we show the quantities $T_{S_{1,i}}$ and $T_{S_{2,i}}$ for an impurity potential centered on a zigzag edge of the flake.

In order to determine the robustness of the influence of impurities on the zigzag edges of a graphene flake on their optical properties, we consider a shorter range impurity potential, as well as a weaker one. In Fig. 10 we plot the absorption spectrum for the W3L11 flake with a zigzag impurity of range $\tau = l_b/5.0$, which corresponds to an impurity potential essentially confined to a single site. It shows that even a shorter range impurity potential centered on the zigzag edge leads to a significant change in the absorption

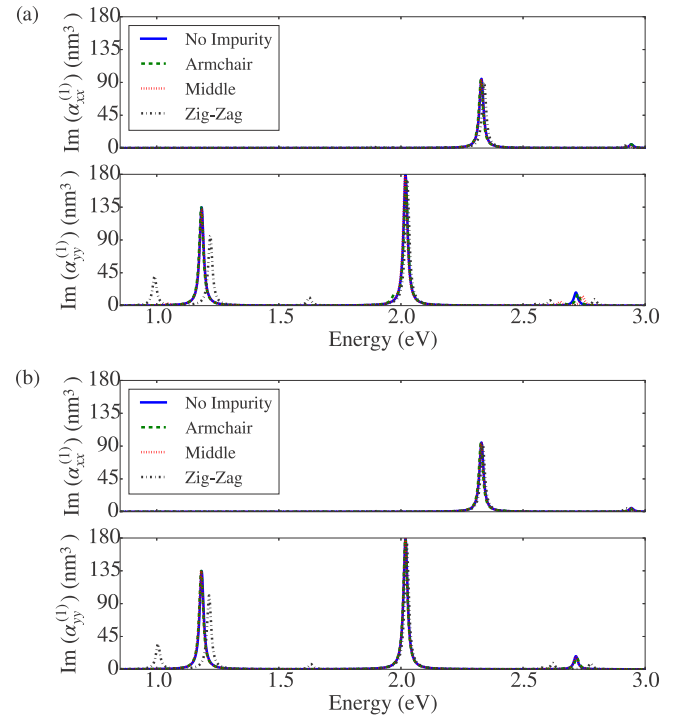


FIG. 10. Absorption spectrum of the W3L11 flake with varied impurity locations, impurity strengths, and ranges. Plot of (a) absorption spectrum for a shorter range impurity potential localized to a particular site with $\bar{\epsilon}_{\max} = t/3$ and $\tau = l_b/5.0$ and (b) the absorption spectrum with a weaker impurity potential, with parameters of $\bar{\epsilon}_{\max} = t/5$ and $\tau = l_b$.

spectrum, as well as in the joint density of states, and they also mix otherwise dark transitions with bright HF excitations. In Fig. 10 we plot the absorption spectrum for the W3L11 flake with a zigzag impurity of reduced strength $\bar{\epsilon}_{\max} = t/5$, while setting the range of influence to $\tau = l_b$. It shows that even a weaker impurity on the zigzag edge has a significant effect on the absorption spectrum of rectangular graphene flakes.

We now analyze a graphene flake with larger zigzag edges than armchair edges, namely the W11L3 flake. In Fig. 11 we plot the absorption spectrum for the W11L3 flake with impurities with potential strength $\bar{\epsilon}_{\max} = t/3$ and range $\tau = l_b$. As we found for the W3L11 flake, an impurity located in the middle of the W11L3 flake, or on its armchair edges, has almost no effect on the absorption spectrum unless the impurity potential extends to the zigzag edges. Impurities located on the zigzag edges, however, can have a significant effect on the absorption spectrum of these flakes. This is because, like the W3L11 flake, the charge distributions involved in the low lying transitions are concentrated on the zigzag edges of the flake. Impurities on the zigzag edges lead to a splitting of the first absorption peak into three smaller ones, and produces a very weak low energy absorption peak corresponding to a transition whose transition dipole moment is polarized along the short (here \hat{y}) axis of the flake. This weak low energy absorption peak is due to a dark transition that becomes mixed with a bright HF single excitation involving the edge modes in the presence of the impurity. In Fig. 12 we show the quantities $T_{S_{1,i}}$, $T_{S_{2,i}}$,

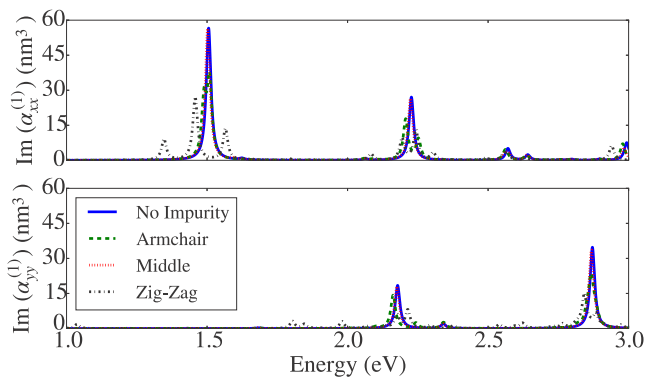


FIG. 11. Absorption spectrum of the W11L3 flake with varied impurity locations. The absorption remains relatively unchanged for impurities located in the middle of the flake, but placing an impurity potential on one of the zigzag edges results in several new peaks. The zigzag impurity potential also induces a very weak, low energy absorption with a transition dipole moment oriented in the \hat{y} direction, the short axis of the flake. The parameters used to model the impurity potential were $\bar{\epsilon}_{\max} = t/3$ and $\tau = l_b$.

$T_{S_3;i}$, and $T_{S_4;i}$ for the W11L3 flake with a zigzag impurity. Much like the pristine graphene flakes, the spatial profiles of these transitions are concentrated on the zigzag edges, but here with reduced electron concentration around the center of the impurity potential. Impurities away from the zigzag edges but with an extended impurity potential that reaches those edges can also impact the optical properties of graphene flakes. In Fig. 13, we show the dependence of the absorption spectrum of the W11L3 flake on the range of the impurity potential as well as strength of the impurity potential. A shorter range impurity potential ($\tau = l_b/5$) on an armchair edge does not change the absorption spectrum, nor does it have a significant effect on the joint density of states, while a shorter range impurity potential on the zigzag flake does. Even a weaker strength impurity potential ($\bar{\epsilon}_{\max} = t/5$) on the zigzag edge leads to a significant change in the absorption spectrum and the joint density of states.

Lastly we analyze the effects of impurities on the larger W9L5 flake. In Fig. 14, we plot the absorption spectrum for a impurity potential with strength $\bar{\epsilon}_{\max} = t/3$, and range $\tau = l_b$, located at different locations on the flake. Again, an impurity on the zigzag edge has a significant effect on the absorption spectrum, while impurities on the armchair edges, or the

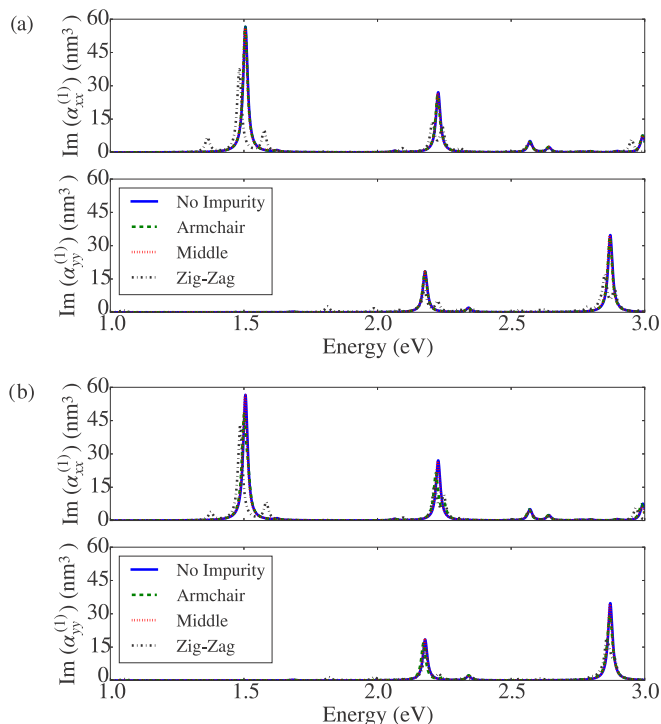


FIG. 13. Absorption spectrum of the W11L3 flake with varied impurity locations, varied impurity strengths, and ranges. Plot of (a) the absorption spectrum of a W11L3 flake with a shorter range impurity potential, parameters used to model the impurity were $\bar{\epsilon}_{\max} = t/3$ and $\tau = l_b/5$ and (b) the absorption spectrum of a W11L3 flake with a weaker impurity potential, parameters used to model the weak impurity potential were $\bar{\epsilon}_{\max} = t/5$ and $\tau = l_b$.

middle of the flake, have almost no impact. This is because the charge distributions involved in the low lying transitions of the system are concentrated mainly on the zigzag edge. The zigzag impurity leads to several peaks within the proximity of the lowest energy absorption peak of the pristine graphene flakes. Similarly to the $WnL3$ family with zigzag impurities, there is a very weak low energy absorption peak associated with a transition whose transition dipole moment is polarized along the short (here \hat{y}) axis of the flake. This peak is associated with a dark transition that becomes mixed with several bright HF excitations, including transitions between edge modes. The impurity potential also significantly enhances (by a factor of

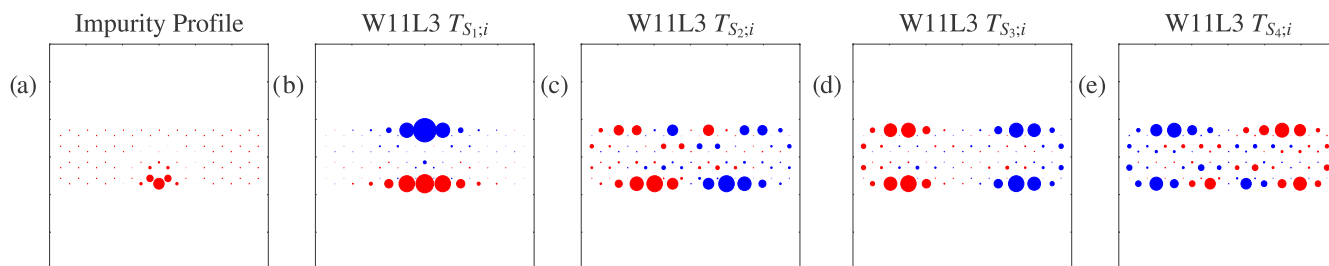


FIG. 12. Plot of the (a) profile of an impurity placed in the zig-zag bottom site of the W11L3 flake with the same parameters as in Fig 11. Plot of (b) $T_{S_1;i}$, (c) $T_{S_2;i}$, (d) $T_{S_3;i}$, and (e) $T_{S_4;i}$ for the W11L3 flake with an impurity potential shown in (a). The charge distributions are still concentrated on the zig-zag edges for these transitions.

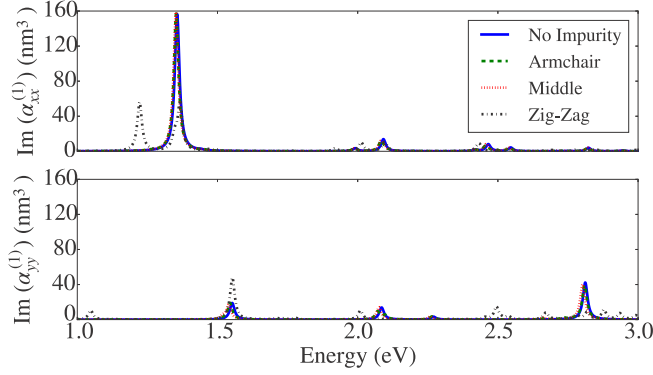


FIG. 14. Absorption spectrum of the W9L5 flake with varied impurity locations. The absorption remains relatively unchanged for impurities located on either the armchair edges or in the middle of the flake. However, placing an impurity potential on one of the zigzag edges results in several new peaks, including a relatively weak low energy absorption which has a transition dipole moment that is polarized in the \hat{y} direction, the short axis of the flake. The parameters used to model the impurity potential were $\bar{\epsilon}_{\max} = t/3$ and $\tau = l_b$.

2.5) the previously weak absorption peak with an associated transition dipole moment polarized along the short (here \hat{y}) axis of the flake by mixing the excited state with several other bright HF excitations. We plot the transition densities $T_{S_{1,i}}$, $T_{S_{2,i}}$, $T_{S_{3,i}}$, and $T_{S_{4,i}}$ in Fig. 15, which shows they are still concentrated on the zigzag edges. In Fig. 16, we explore the dependence of the absorption spectrum on the strength of the impurity potential. Even a weaker impurity potential placed on the zigzag edge can have a significant impact on the absorption spectrum.

Ultimately, impurities on the zigzag edge have a significant effect on the low energy absorption spectrum of the graphene flakes studied in this paper. This is because the charge distributions involved in the low energy transitions are concentrated on the zigzag edges. Impurities located in the middle of the flake, or on the armchair edges, have essentially no impact as they do not affect the charge distributions involved in the low energy transitions in these systems. Even though the impurity potential can often lead to the shift of the energies of peaks, and can turn dark transitions bright, it can sometimes enhance certain absorption features, making the role of impurities potentially beneficial to certain applications.

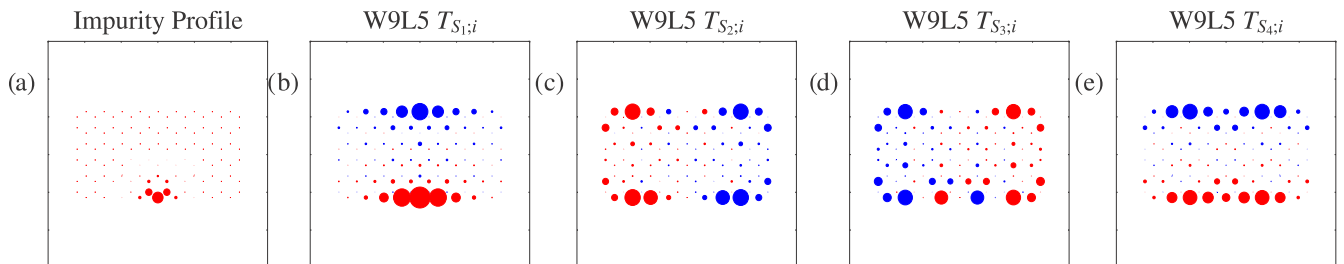


FIG. 15. Plot of (a) the profile of an impurity placed in the zigzag bottom site of the W9L5 flake with the same parameter as Fig. 14. Plot of (b) $T_{S_{1,i}}$, (c) $T_{S_{2,i}}$, (d) $T_{S_{3,i}}$, and (e) $T_{S_{4,i}}$ for the W9L5 flake with an impurity potential from (a). The charge distributions are still concentrated on the zigzag edges for these transitions.

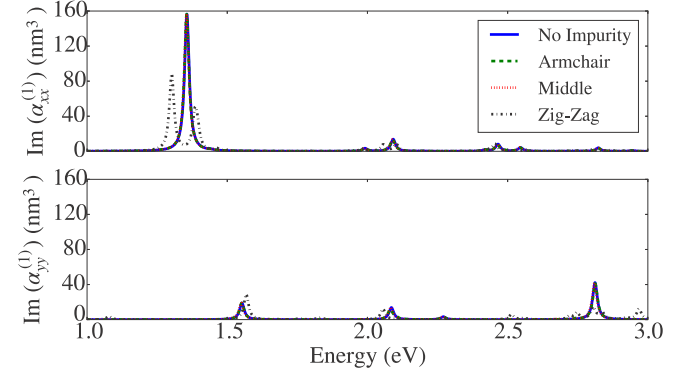


FIG. 16. Absorption spectrum of the W9L5 flake with varied impurity locations and a weaker strength. The parameters used to model the impurity potential were $\bar{\epsilon}_{\max} = t/5$ and $\tau = l_b$.

V. CONCLUSION

We have calculated the optical properties of several rectangular graphene flakes, taking into account electron correlations beyond the mean-field level. Including these correlations is essential to accurately describe the low energy optical absorption of these flakes, as mean-field theory alone cannot accurately predict their optical properties. We find that the first absorption peak invariably corresponds to a transition dipole moment polarized along the longest axis of the flake. We also find that the electron concentration for the low energy transitions are always concentrated on the zigzag edges, regardless of whether or not the zigzag edges are longer than the armchair edges. Thus, similarly to graphene nanoribbons, the zigzag edges of rectangular graphene flakes plays a primary role in the optical absorption, even for very small graphene flakes. Recent progress in the synthesis of rectangular graphene flakes [52] holds promise for producing graphene flakes of desired shapes and sizes. Predictions of optical properties of graphene flakes, such as those presented in this paper, could be tested by measuring the absorption spectra of graphene flakes either in solution or deposited on substrates.

We also investigated the effect of impurities on the optical properties of rectangular graphene flakes by placing impurity potentials of different spatial ranges and strengths on different locations. We find that the effect of impurities on the optical properties of these graphene flakes strongly depends on the location of the impurity potential. Impurities on the zigzag

edges have a significant impact on the optical properties of these graphene flakes, while impurities on the “bulk” region or their armchair edges have a negligible impact on the frequencies and the nature of the optical transitions. We expect that understanding these qualitative features will be central in the design of any graphene flake devices, both when it is desirable to avoid the effects of impurities, and when it is desirable to exploit their effect on the optical properties of the graphene flakes.

APPENDIX: FULL HAMILTONIAN IN THE ELECTRON/HOLE BASIS

In this appendix, we rewrite the total Hamiltonian in the electron-hole basis, which is an important step in our configuration interaction calculations (16).

1. The tight-binding and impurity Hamiltonian in the electron/hole basis

The tight-binding Hamiltonian (2), combined with the impurity potential (5), can be written as

$$H_{TB} + H_{\text{imp}} = -t \sum_{(i,j),\sigma} c_{i\sigma}^\dagger c_{j\sigma} + \sum_{i\sigma} \bar{\epsilon}_i c_{i\sigma}^\dagger c_{i\sigma}. \quad (\text{A1})$$

Moving to the basis defined in (10,11), this Hamiltonian can be written as

$$H_{TB} + H_{\text{imp}} = \sum_{mm'\sigma} \tilde{\kappa}_{mm'} C_{m\sigma}^\dagger C_{m'\sigma}, \quad (\text{A2})$$

where

$$\tilde{\kappa}_{mm'} = \sum_i \bar{\epsilon}_i M_{m\sigma,i} M_{m'\sigma,i}^* - t \sum_{(i,j)} M_{m\sigma,i} M_{m'\sigma,j}^*. \quad (\text{A3})$$

$$\begin{aligned} H_{Hu;1} = & \sum_{\substack{mm' \\ p \in \text{filled}}} \Gamma_{mm'pp} a_{m\uparrow}^\dagger a_{m'\uparrow} + \sum_{\substack{pp' \\ m \in \text{filled}}} \Gamma_{mmp'p} a_{p\downarrow}^\dagger a_{p'\downarrow} - \sum_{\substack{pp' \\ m \in \text{filled}}} \Gamma_{mmp'p} b_{p'\uparrow}^\dagger b_{p\uparrow} - \sum_{\substack{mm' \\ p \in \text{filled}}} \Gamma_{mm'pp} b_{m'\downarrow}^\dagger b_{m\downarrow} \\ & + \sum_{\substack{mm' \\ p \in \text{filled}}} \Gamma_{mm'pp} a_{m\uparrow}^\dagger b_{m'\downarrow}^\dagger + \sum_{\substack{pp' \\ m \in \text{filled}}} \Gamma_{mmp'p} a_{p\downarrow}^\dagger b_{p'\uparrow}^\dagger + \sum_{\substack{mm' \\ p \in \text{filled}}} \Gamma_{mm'pp} b_{m\downarrow} a_{m'\uparrow} + \sum_{\substack{pp' \\ m \in \text{filled}}} \Gamma_{mmp'p} b_{p\uparrow} a_{p'\downarrow}. \end{aligned} \quad (\text{A10})$$

Equation (A10) contains the single particle terms that play a role in the matrix elements of both single and double excitations. The third part of the Hubbard Hamiltonian is

$$\begin{aligned} H_{Hu;2} = & \sum_{mm'pp'} \Gamma_{mm'pp'} (a_{p\downarrow}^\dagger b_{m\downarrow} - a_{m\uparrow}^\dagger b_{p\uparrow}) a_{m'\uparrow} a_{p'\downarrow} + \sum_{mm'pp'} \Gamma_{mm'pp'} a_{m\uparrow}^\dagger a_{p\downarrow}^\dagger (b_{p'\uparrow} a_{m'\uparrow} - b_{m'\downarrow} a_{p'\downarrow}) \\ & + \sum_{mm'pp'} \Gamma_{mm'pp'} (b_{m'\downarrow}^\dagger a_{p'\downarrow} - b_{p'\uparrow}^\dagger a_{m'\uparrow}) b_{p\uparrow} b_{m\downarrow} + \sum_{mm'pp'} \Gamma_{mm'pp'} b_{m'\downarrow}^\dagger b_{p'\uparrow}^\dagger (a_{p\downarrow}^\dagger b_{m\downarrow} - a_{m\uparrow}^\dagger b_{p\uparrow}). \end{aligned} \quad (\text{A11})$$

Equation (A11) has matrix elements between single and double excitations. The fourth part of the Hubbard Hamiltonian is

$$\begin{aligned} H_{Hu;3} = & - \sum_{mm'pp'} \Gamma_{mm'pp'} (a_{p\downarrow}^\dagger b_{m'\downarrow}^\dagger b_{m\downarrow} a_{p'\downarrow} + a_{m\uparrow}^\dagger b_{p'\uparrow}^\dagger b_{p\uparrow} a_{m'\uparrow}) + \sum_{mm'pp'} \Gamma_{mm'pp'} (a_{p\downarrow}^\dagger b_{p'\uparrow}^\dagger b_{m\downarrow} a_{m'\uparrow} + a_{m\uparrow}^\dagger b_{m'\downarrow}^\dagger b_{p\uparrow} a_{p'\downarrow}) \\ & - \sum_{mm'pp'} \Gamma_{mm'pp'} (b_{m\downarrow} b_{p\uparrow} a_{m'\uparrow} a_{p'\downarrow} + a_{m\uparrow}^\dagger a_{p\downarrow}^\dagger b_{m'\downarrow}^\dagger b_{p'\uparrow}^\dagger). \end{aligned} \quad (\text{A12})$$

Then, we can rewrite (A2) in the electron-hole basis (13) as

$$\begin{aligned} H_{TB} + H_{\text{imp}} = & \sum_{mm'\sigma} \tilde{\kappa}_{mm'} a_{m\sigma}^\dagger a_{m'\sigma} - \sum_{mm'\sigma} \tilde{\kappa}_{mm'} b_{m'\sigma}^\dagger b_{m\sigma} \\ & + \sum_{mm'\sigma} \tilde{\kappa}_{mm'} (a_{m\sigma}^\dagger b_{m'\sigma}^\dagger + b_{m\sigma} a_{m'\sigma}) \\ & + \sum_{m\sigma} \tilde{\kappa}_{mm\sigma}. \end{aligned} \quad (\text{A4})$$

2. The Hubbard Hamiltonian in the electron/hole basis

The Hubbard Hamiltonian (3) can be written as

$$H_{Hu} = U \sum_i n_{i\uparrow} n_{i\downarrow}. \quad (\text{A5})$$

In the basis defined in (10,11), we can write this as

$$H_{Hu} = \sum_{mm'pp'} \Gamma_{mm'pp'} C_{m\uparrow}^\dagger C_{m'\uparrow} C_{p\downarrow}^\dagger C_{p'\downarrow}, \quad (\text{A6})$$

where

$$\Gamma_{mm'pp'} = U \sum_i M_{m\uparrow,i} M_{m'\uparrow,i}^* M_{p\downarrow,i} M_{p'\downarrow,i}^*. \quad (\text{A7})$$

Moving to an electron-hole basis, the Hubbard Hamiltonian can be written as

$$H_{Hu} = H_{Hu;0} + H_{Hu;1} + H_{Hu;2} + H_{Hu;3} + H_{Hu;4}. \quad (\text{A8})$$

The first term can be written as

$$H_{Hu;0} = \sum_{\substack{m \in \text{filled} \\ n \in \text{filled}}} \Gamma_{mmnn}. \quad (\text{A9})$$

Equation (A9) accounts for the Coulomb repulsion of the nominal vacuum.

The second part of the Hamiltonian is

Equation (A12) is the part of the Hamiltonian that has a contribution to the matrix elements between single excitations, between the ground state and double excitations, as well as between different double excitations. The last part of the Hubbard Hamiltonian is

$$H_{Hu;4} = \sum_{mm'pp'} \Gamma_{mm'pp'} a_{p\downarrow}^\dagger a_{m\uparrow}^\dagger a_{m'\uparrow} a_{p'\downarrow} + \sum_{mm'pp'} \Gamma_{mm'pp'} b_{m'\downarrow}^\dagger b_{p'\uparrow}^\dagger b_{p\uparrow} b_{m\downarrow}. \quad (\text{A13})$$

The term (A13) has matrix elements between double excitations only.

3. The extended Hubbard Hamiltonian in the electron/hole basis

The extended Hubbard Hamiltonian can be written as

$$H_{\text{ext}} = H_{ee} + H_{en} + H_{nn}, \quad (\text{A14})$$

where

$$H_{ee} = \frac{1}{2} \sum_{\substack{i \neq j \\ \sigma \sigma'}} V_{ij} n_{i\sigma} n_{j\sigma'}, \quad (\text{A15})$$

$$H_{en} = -\frac{1}{2} \sum_{\substack{i \neq j \\ \sigma}} V_{ij} (n_{i\sigma} + n_{j\sigma}), \quad (\text{A16})$$

$$H_{nn} = \frac{1}{2} \sum_{i \neq j} V_{ij}. \quad (\text{A17})$$

The term (A15) describes the long-range interaction between the electrons, (A16) describes the electron-nuclei interaction,

and the term (A17) describes the nuclei-nuclei interaction, which in our model is a constant.

a. H_{ee} in the electron/hole basis

The extended Hubbard electron-electron repulsion Hamiltonian is

$$H_{ee} = \frac{1}{2} \sum_{i \neq j \sigma \sigma'} V_{ij} n_{i\sigma} n_{j\sigma'}. \quad (\text{A18})$$

Rewriting this in the HF basis,

$$H_{ee} = \sum_{\substack{mm'nn' \\ \sigma \sigma'}} \Phi_{mm'nn'} C_{m\sigma}^\dagger C_{m'\sigma'} C_{n\sigma}^\dagger C_{n'\sigma'}, \quad (\text{A19})$$

where

$$\Phi_{mm'nn'} = \frac{1}{2} \sum_{i \neq j} V_{ij} M_{m\sigma,i} M_{n'\sigma',i}^* M_{n\sigma',j} M_{m'\sigma,j}^*. \quad (\text{A20})$$

Moving to the electron-hole basis and normal ordering, the Hamiltonian can be written as

$$H_{ee} = H_{ee;0} + H_{ee;1} + H_{ee;2} + H_{ee;3} + H_{ee;4}. \quad (\text{A21})$$

The first part of the Hamiltonian can be written as

$$H_{ee;0} = \sum_{\substack{\sigma \sigma' \\ m, n \in \text{filled}}} \Phi_{mnnn} + \sum_{\substack{m \in \text{filled} \\ n \in \text{unfilled} \\ \sigma}} \Phi_{mnnm}. \quad (\text{A22})$$

The term $H_{ee;0}$ (A22) represents the long-range Coulomb repulsion of the initial ground state. The second part of the Hamiltonian is

$$\begin{aligned} H_{ee;1} = & \sum_{\substack{mn'\sigma \\ n \in \text{unfilled}}} \Phi_{mnnn'} a_{m\sigma}^\dagger a_{n'\sigma} - \sum_{\substack{nn'\sigma\sigma' \\ m \in \text{filled}}} \Phi_{mnnn'} b_{n'\sigma}^\dagger b_{n\sigma} - \sum_{\substack{mm'\sigma\sigma' \\ n \in \text{filled}}} \Phi_{mnnn'} b_{m'\sigma}^\dagger b_{m\sigma} + \sum_{\substack{m'n\sigma \\ m \in \text{filled}}} \Phi_{mnnm'} b_{m'\sigma}^\dagger b_{n\sigma} \\ & + \sum_{\substack{mn'\sigma \\ n \in \text{unfilled}}} \Phi_{mnnn'} a_{m\sigma}^\dagger b_{n'\bar{\sigma}}^\dagger + \sum_{\substack{mn'\sigma \\ n \in \text{unfilled}}} \Phi_{mnnn'} b_{m\bar{\sigma}} a_{n'\sigma} + \sum_{\substack{mm'\sigma\sigma' \\ n \in \text{filled}}} \Phi_{mnnn'} a_{m\sigma}^\dagger a_{m'\sigma} - \sum_{\substack{mn'\sigma \\ n \in \text{unfilled}}} \Phi_{mnnn'} b_{n'\sigma}^\dagger b_{m\sigma} \\ & + \sum_{\substack{nn'\sigma\sigma' \\ m \in \text{filled}}} \Phi_{mnnn'} a_{n\sigma}^\dagger a_{n'\sigma} - \sum_{\substack{m'n\sigma \\ m \in \text{filled}}} \Phi_{mnnm'} a_{n\sigma}^\dagger a_{m'\sigma} + \sum_{\substack{mm'\sigma\sigma' \\ n \in \text{filled}}} \Phi_{mnnn'} a_{m\sigma}^\dagger b_{m'\bar{\sigma}}^\dagger + \sum_{\substack{mm'\sigma\sigma' \\ n \in \text{filled}}} \Phi_{mnnn'} b_{m\bar{\sigma}} a_{m'\sigma} \\ & + \sum_{\substack{m'n\sigma \\ m \in \text{filled}}} \Phi_{mnnm'} a_{m'\sigma} b_{n\bar{\sigma}} + \sum_{\substack{nn'\sigma\sigma' \\ m \in \text{filled}}} \Phi_{mnnn'} a_{n\sigma}^\dagger b_{n'\bar{\sigma}}^\dagger + \sum_{\substack{m'n\sigma \\ m \in \text{filled}}} \Phi_{mnnm'} b_{m'\bar{\sigma}}^\dagger a_{n\sigma}^\dagger + \sum_{\substack{nn'\sigma\sigma' \\ m \in \text{filled}}} \Phi_{mnnn'} b_{n\bar{\sigma}} a_{n'\sigma}. \end{aligned} \quad (\text{A23})$$

The term $H_{ee;1}$ (A23) represents the single-particle terms that play a role in the matrix elements of both single and double excitations. The third part of the Hamiltonian is

$$\begin{aligned} H_{ee;2} = & \sum_{mm'nn'\sigma\sigma'} \Phi_{mnnn'} a_{m\sigma}^\dagger a_{n\sigma'}^\dagger b_{n'\bar{\sigma}}^\dagger a_{m'\sigma} + \sum_{mm'nn'\sigma\sigma'} \Phi_{mnnn'} a_{m\sigma}^\dagger a_{n'\sigma'} a_{m'\sigma} b_{n\bar{\sigma}} + \sum_{mm'nn'\sigma\sigma'} \Phi_{mnnn'} a_{n\sigma}^\dagger a_{m\sigma}^\dagger b_{m'\bar{\sigma}}^\dagger a_{n'\sigma'} \\ & + \sum_{mm'nn'\sigma\sigma'} \Phi_{mnnn'} a_{n\sigma}^\dagger b_{m\bar{\sigma}} a_{m'\sigma} a_{n'\sigma'} + \sum_{mm'nn'\sigma\sigma'} \Phi_{mnnn'} a_{m\sigma}^\dagger b_{n'\sigma'}^\dagger b_{m'\bar{\sigma}}^\dagger b_{n\sigma'} + \sum_{mm'nn'\sigma\sigma'} \Phi_{mnnn'} b_{n'\sigma'}^\dagger a_{m'\sigma} b_{m\bar{\sigma}} b_{n\sigma'} \\ & + \sum_{mm'nn'\sigma\sigma'} \Phi_{mnnn'} b_{m'\sigma}^\dagger b_{n'\bar{\sigma}}^\dagger a_{n\sigma}^\dagger b_{m\sigma} - \sum_{mm'nn'\sigma\sigma'} \Phi_{mnnn'} b_{m'\sigma}^\dagger b_{m\sigma} b_{n\bar{\sigma}} a_{n'\sigma'}. \end{aligned} \quad (\text{A24})$$

The term $H_{ee;2}$ (A24) can have nonzero matrix elements between single and double excitations. The fourth part of the Hamiltonian is

$$H_{ee;3} = - \sum_{mm'nn'\sigma\sigma'} \Phi_{mm'nn'} a_{m\sigma}^\dagger b_{n'\sigma'}^\dagger b_{n\sigma'} a_{m'\sigma} - \sum_{mm'nn'\sigma\sigma'} \Phi_{mm'nn'} a_{n\sigma'}^\dagger b_{m'\sigma}^\dagger b_{m\sigma} a_{n'\sigma'} + \sum_{mm'nn'\sigma\sigma'} \Phi_{mm'nn'} a_{m\sigma}^\dagger b_{m'\bar{\sigma}}^\dagger b_{n\bar{\sigma}} a_{n'\sigma'} + \sum_{mm'nn'\sigma\sigma'} \Phi_{mm'nn'} a_{n\sigma'}^\dagger b_{n'\bar{\sigma}}^\dagger b_{m\bar{\sigma}} a_{m'\sigma} + \sum_{mm'nn'\sigma\sigma'} \Phi_{mm'nn'} b_{m\bar{\sigma}} a_{m'\sigma} b_{n\bar{\sigma}} a_{n'\sigma'} + \sum_{mm'nn'\sigma\sigma'} \Phi_{mm'nn'} a_{m\sigma}^\dagger b_{m'\bar{\sigma}}^\dagger a_{n\sigma'}^\dagger b_{n'\bar{\sigma}}^\dagger. \quad (\text{A25})$$

The term $H_{ee;3}$ (A25) contributes to the matrix elements between single excitations, between the ground state and double excitations, as well as between different double excitations. The fifth part of the Hamiltonian is

$$H_{ee;4} = \sum_{mm'nn'\sigma\sigma'} \Phi_{mm'nn'} a_{n\sigma'}^\dagger a_{m\sigma}^\dagger a_{m'\sigma} a_{n'\sigma'} + \sum_{mm'nn'\sigma\sigma'} \Phi_{mm'nn'} b_{n'\sigma'}^\dagger b_{m'\sigma}^\dagger b_{m\sigma} b_{n\sigma'}. \quad (\text{A26})$$

The term $H_{ee;4}$ (A26) contributes to the matrix elements between double excitations only.

b. H_{en} in the electron/hole basis

The electron-nuclei Hamiltonian is given by

$$H_{en} = -\frac{1}{2} \sum_{i \neq j, \sigma} V_{ij} (n_{i\sigma} + n_{j\sigma}). \quad (\text{A27})$$

In the basis defined in (10,11), this is

$$H_{en} = \sum_{mm'\sigma} \bar{\phi}_{mm'} C_{m\sigma}^\dagger C_{m'\sigma}, \quad (\text{A28})$$

where

$$\bar{\phi}_{mm'} = -\frac{1}{2} \sum_{i \neq j} V_{ij} (M_{m\sigma, i} M_{m'\sigma, j} + M_{m\sigma, j} M_{m'\sigma, i}^*). \quad (\text{A29})$$

Moving to the electron-hole basis, we can write (A28) as

$$H_{en} = \sum_{m \in \text{filled}, \sigma} \bar{\phi}_{mm} + \sum_{mm'\sigma} \bar{\phi}_{mm'} a_{m\sigma}^\dagger a_{m'\sigma} + \sum_{mm'\sigma} \bar{\phi}_{mm'} a_{m\sigma}^\dagger b_{m'\bar{\sigma}} + \sum_{mm'\sigma} \bar{\phi}_{mm'} b_{m\bar{\sigma}} a_{m'\sigma} - \sum_{mm'\sigma} \bar{\phi}_{mm'} b_{m'\sigma}^\dagger b_{m\sigma}. \quad (\text{A30})$$

The electron-nuclei interaction (A30) contributes to matrix elements between single excitations, matrix elements between double excitations, and matrix elements between single and double excitations and single excitations and the nominal vacuum.

- [1] K. S. Novoselov, A. K. Geim, S. V. Morozov, D. Jiang, Y. Zhang, S. V. Dubonos, I. V. Grigorieva, and A. A. Firsov, *Science* **306**, 666 (2004).
- [2] K. S. Novoselov, A. K. Geim, S. V. Morozov, D. Jiang, M. I. Katsnelson, I. V. Grigorieva, S. V. Dubonos, and A. A. Firsov, *Nature (London)* **438**, 197 (2005).
- [3] Y. Zhang, Y.-W. Tan, H. L. Stormer, and P. Kim, *Nature (London)* **438**, 201 (2005).
- [4] A. Rycerz, J. Tworzydło, and C. W. J. Beenakker, *Nat. Phys.* **3**, 172 (2007).
- [5] C. Lee, X. Wei, J. W. Kysar, and J. Hone, *Science* **321**, 385 (2008).
- [6] D. A. Dikin, S. Stankovich, E. J. Zimney, R. D. Piner, G. H. B. Dommett, G. Evmenenko, S. T. Nguyen, and R. S. Ruoff, *Nature (London)* **448**, 457 (2007).
- [7] G. Xin, T. Yao, H. Sun, S. Scott, D. Shao, G. Wang, and J. Lian, *Science* **349**, 1083 (2015).
- [8] K. F. Mak, M. Y. Sfeir, Y. Wu, C. H. Lui, J. A. Misewich, and T. F. Heinz, *Phys. Rev. Lett.* **101**, 196405 (2008).
- [9] Y. Zhang, T. T. Tang, C. Girit, Z. Hao, M. C. Martin, A. Zettl, M. F. Crommie, Y. R. Shen, and F. Wang, *Nature (London)* **459**, 820 (2009).
- [10] J. Mao, Y. Jiang, D. Moldovan, G. Li, K. Watanabe, T. Taniguchi, M. R. Masir, F. M. Peeters, and E. Y. Andrei, *Nat. Phys.* **12**, 545 (2016).
- [11] Q. Bao, H. Zhang, Y. Wang, Z. Ni, Y. Yan, Z. X. Shen, K. P. Loh, and D. Y. Tang, *Adv. Func. Mat.* **19**, 3077 (2009).
- [12] J. W. Kim, S. Y. Choi, B. H. Jung, D.-I. Yeom, and F. Rotermund, *Appl. Phys. Exp.* **6**, 032704 (2013).
- [13] B. V. Cunning, C. L. Brown, and D. Kieplinski, *Appl. Phys. Lett.* **99**, 261109 (2011).
- [14] Q.-W. Sheng, M. Feng, W. Xin, H. Guo, T.-Y. Han, Y.-G. Li, Y.-G. Liu, F. Gao, F. Song, Z.-B. Liu, and J.-G. Tian, *Appl. Phys. Lett.* **105**, 041901 (2014).
- [15] Q. Bao, H. Zhang, B. Wang, Z. Ni, C. H. Y. X. Lim, Y. Wang, D. Y. Tang, and K. P. Loh, *Nat. Photon.* **5**, 411 (2011).
- [16] H. Zhang, D. Y. Tang, L. M. Zhao, Q. Bao, and K. P. Loh, *Opt. Express* **17**, 17630 (2009).
- [17] A. H. C. Neto, F. Guinea, N. M. R. Peres, K. S. Novoselov, and A. K. Geim, *Rev. Mod. Phys.* **81**, 109 (2009).
- [18] S. Dutta and S. K. Pati, *J. Mat. Chem.* **20**, 8207 (2010).
- [19] K. Wakabayashi, K. Sasaki, T. Nakanishi, and T. Enoki, *Sci. Technol. Adv. Mater.* **11**, 054504 (2010).
- [20] W. Jaskólski, A. Ayuela, M. Pelc, H. Santos, and L. Chico, *Phys. Rev. B* **83**, 235424 (2011).
- [21] M. Buzaglo, M. Shtein, and O. Regev, *Chem. Mat.* **28**, 21 (2016).
- [22] I. Ozfidan, M. Korkusinski, A. D. Güçlü, J. A. McGuire, and P. Hawrylak, *Phys. Rev. B* **89**, 085310 (2014).
- [23] H. Riesen, C. Wiebeler, and S. Schumacher, *J. Phys. Chem. A* **118**, 5189 (2014).

- [24] C. Sun, F. Figge, I. Ozfidan, M. Korkusinski, X. Yan, L.-S. Li, P. Hawrylak, and J. A. McGuire, *Nano Lett.* **15**, 5472 (2015).
- [25] L. Liao, Y. C. Lin, M. Bao, R. Cheng, J. Bai, Y. Liu, Y. Qu, K. L. Wang, Y. Huang, and X. Duan, *Nature (London)* **467**, 305 (2010).
- [26] Y. M. Lin, C. Dimitrakopoulos, K. A. Jenkins, D. B. Farmer, H. Y. Chiu, A. Grill, and P. Avouris, *Science* **327**, 662 (2010).
- [27] M. B. Smith and J. Michl, *Ann. Rev. Phys. Chem.* **64**, 361 (2013).
- [28] I. Paci, J. Johnson, X. Chen, G. Rana, D. Popovic, D. David, A. Nozik, M. Ratner, and J. Michl, *J. Am. Chem. Soc.* **128**, 16546 (2006).
- [29] S.-H. Choi, *J. Phys. D: Appl. Phys.* **50**, 103002 (2017).
- [30] K. Li, W. Liu, Y. Ni, D. Li, D. Lin, Z. Su, and G. Wei, *J. Mat. Chem. B* **5**, 4811 (2017).
- [31] C. Salazar, J. L. Cheng, and J. E. Sipe, *Phys. Rev. B* **93**, 075442 (2016).
- [32] J. L. Cheng, N. Vermeulen, and J. E. Sipe, *New J. Phys.* **16**, 053014 (2014).
- [33] J. L. Cheng, N. Vermeulen, and J. E. Sipe, *Phys. Rev. B* **91**, 235320 (2015).
- [34] J. L. Cheng, N. Vermeulen, and J. E. Sipe, *Sci. Rep.* **7**, 43843 (2017).
- [35] Y. Li, H. Shu, S. Wang, and J. Wang, *J. Phys. Chem. C* **119**, 4983 (2015).
- [36] S. Thongrattanasiri, A. Manjavacas, and F. J. G. de Abajo, *ACS Nano* **6**, 1766 (2012).
- [37] Z. Z. Zhang, K. Chang, and F. M. Peeters, *Phys. Rev. B* **77**, 235411 (2008).
- [38] L. L. Li, M. Zarenia, W. Xu, H. M. Dong, and F. M. Peeters, *Phys. Rev. B* **95**, 045409 (2017).
- [39] R. A. Muniz, H. P. Dahal, A. V. Balatsky, and S. Haas, *Phys. Rev. B* **82**, 081411 (2010).
- [40] H. P. Dahal, R. A. Muniz, S. Haas, M. J. Graf, and A. V. Balatsky, *Philos. Mag.* **91**, 4276 (2011).
- [41] Y. C. Chang and S. Haas, *Phys. Rev. B* **83**, 085406 (2011).
- [42] R. V. Pottelberge, M. Zarenia, P. Vasilopoulos, and F. M. Peeters, *Phys. Rev. B* **95**, 245410 (2017).
- [43] P. Potasz, A. D. Güçlü, A. Wójs, and P. Hawrylak, *Phys. Rev. B* **85**, 075431 (2012).
- [44] I. Ozfidan, M. Korkusinski, and P. Hawrylak, *Phys. Rev. B* **91**, 115314 (2015).
- [45] I. Ozfidan, M. Korkusinski, and P. Hawrylak, *Phys. Status Solidi RRL* **10**, 13 (2016).
- [46] I. Ozfidan, A. D. Güçlü, and P. Hawrylak, *Phys. Status Solidi RRL* **10**, 102 (2016).
- [47] Y. Lu, W. Lu, W. Liang, and H. Liu, *Phys. Rev. B* **88**, 165425 (2013).
- [48] Y. Lu, S. Wei, J. Ji, W. Lu, and L. Wang, *J. Appl. Phys.* **120**, 204301 (2016).
- [49] Y. Lu, S. Wei, J. Jin, W. Lu, and L. Wang, *New J. Phys.* **18**, 123033 (2016).
- [50] C. M. Wettstein, F. P. Bonafé, M. B. Oviedo, and C. G. Sánchez, *J. Chem. Phys.* **144**, 244305 (2016).
- [51] A. Altıntaş, K. E. Çakmak, and A. D. Güçlü, *Phys. Rev. B* **95**, 045431 (2017).
- [52] C. Rogers, C. Chen, Z. Pedramrazi, A. A. Omrani, H.-Z. Tsai, H. S. Jung, S. Lin, M. F. Crommie, and F. R. Fischer, *Angew. Chem. Int. Ed.* **54**, 15143 (2015).
- [53] J. Vergés, G. Chiappe, and E. Louis, *Eur. Phys. J. B* **88**, 200 (2015).
- [54] J. A. Vergés, G. Chiappe, and E. Louis, [arXiv:1612.06667](https://arxiv.org/abs/1612.06667).
- [55] C. H. A. Wong, Z. Sofer, M. Kubešová, J. Kučera, S. Matějková, and M. Pumera, *PNAS* **111**, 13774 (2014).
- [56] T. Latychevskaia, F. Wicki, C. Escher, and H.-W. Fink, *Ultramicroscopy* **182**, 276 (2017).
- [57] R. Pariser and R. G. Parr, *J. Chem. Phys.* **21**, 466 (1953).
- [58] R. Pariser and R. G. Parr, *J. Chem. Phys.* **21**, 767 (1953).
- [59] J. A. Pople, *Proc. Phys. Soc.* **68**, 81 (1954).
- [60] T. Brown, *Chemistry, The Central Science* (Prentice Hall, New York, 2011).
- [61] J. Platt, *Free-Electron Theory of Conjugated Molecules: A Source Book* (John Wiley, New York, 1964).
- [62] V. M. Agranovich, *Excitations in Organic Solids* (Oxford University Press, New York, 2009).
- [63] C. Raghu, Y. A. Pati, and S. Ramasesha, *Phys. Rev. B* **66**, 035116 (2002).
- [64] C. Raghu, Y. A. Pati, and S. Ramasesha, *Phys. Rev. B* **65**, 155204 (2002).
- [65] W. Barford, *Electronic and Optical Properties of Conjugated Polymers*, 1st ed. (Oxford University Press, New York, 2005).
- [66] R. Kundu, *Mod. Phys. Lett. B* **25**, 163 (2011).
- [67] J. Hachmann, J. Dorando, M. Aviles, and G. K.-L. Chan, *J. Chem. Phys.* **127**, 134309 (2007).
- [68] T. O. Wehling, E. Şaşıoğlu, C. Friedrich, A. I. Lichtenstein, M. I. Katsnelson, and S. Blügel, *Phys. Rev. Lett.* **106**, 236805 (2011).
- [69] M. Schuler, M. Rosner, T. O. Wehling, A. I. Lichtenstein, and M. I. Katsnelson, *Phys. Rev. Lett.* **111**, 036601 (2013).
- [70] W. Wu and A.-M. S. Tremblay, *Phys. Rev. B* **89**, 205128 (2014).
- [71] S. Arya, P. V. Sriluckshmy, S. R. Hassan, and A.-M. S. Tremblay, *Phys. Rev. B* **92**, 045111 (2015).
- [72] L. M. Martelo, M. Dzierzawa, L. Siffert, and D. Baeriswyl, *Z. Phys. B* **103**, 335 (1997).
- [73] X.-Y. Wang, A. Narita, W. Zhang, X. Feng, and K. Müllen, *J. Am. Chem. Soc.* **138**, 9021 (2016).
- [74] X.-Y. Wang, T. Dienel, M. D. Giovannantonio, G. B. Barin, N. Khariche, O. Deniz, J. I. Urgel, R. Widmer, S. Stolz, L. H. D. Lima, M. Muntwiler, M. Tommasini, V. Meunier, P. Ruffieux, X. Feng, R. Fasel, K. Müllen, and A. Narita, *J. Am. Chem. Soc.* **139**, 4671 (2017).
- [75] H. Bruus and K. Flensberg, *Many-body Quantum Theory in Condensed Matter Physics* (Oxford University Press, New York, 2004).
- [76] G. F. Giuliani and G. Vignale, *Quantum Theory of the Electron Liquid* (Cambridge University Press, New York, 2005).
- [77] D. Pines, *Elementary Excitations in Solids* (W.A. Benjamin Inc., New York, 1977).
- [78] S. Sorella and E. Tosatti, *Europhys. Lett.* **19**, 699 (1992).
- [79] J.-P. Malrieu and G. Trinquier, *J. Phys. Chem. A* **120**, 9564 (2016).
- [80] F. Plasser, H. Pašalić, M. H. Gerzabek, F. Libisch, R. Reiter, J. Burgdörfer, T. Müller, R. Shepard, and H. Lischka, *Angew. Chem. Int. Ed.* **52**, 2581 (2013).
- [81] I. Hagymási and O. Legeza, *Phys. Rev. B* **94**, 165147 (2016).
- [82] F. Moscardó and E. San-Fabián, *Chem. Phys. Lett.* **480**, 26 (2009).
- [83] E. San-Fabián and F. Moscardó, *Eur. Phys. J. D* **64**, 239 (2011).
- [84] R. Boyd, *Nonlinear Optics* (Academic Press Inc., San Diego, 2008).
- [85] Z. S. Sadeq and J. E. Sipe, [arXiv:1511.09396](https://arxiv.org/abs/1511.09396).